Transactions of the **14th International Conference on Structural Mechanics in Reactor Technology** (SMiRT 14), Lyon, France, August 17-22, 1997

GW/7

On the simulation of ductile crack growth using the Rousselier model

Poussard C.[(1)], **Seidenfuss M.**[(2)]
(1) CEA, France
(2) MPA Universität Stuttgart, Germany

ABSTRACT

The Rousselier model as modified by Seidenfuss and implemented in CASTEM 2000 was used to investigate ductile crack growth in CT25 specimens made of 20 MnMoNi 5 5 material. The procedure employed to determine the damage parameters is briefly reviewed. The ability of the model to describe crack growth in 3D for varying stress state triaxiality conditions is investigated. J-Δa curves derived from the calculations are found to be in good agreement with the experimental observations.

1 INTRODUCTION

It is well known that both the deviatoric stress component and the stress triaxiality are decisive factors affecting the failure behaviour of materials [1]. Classic approaches, based on the Von Mises theory, do not take the influence of the hydrostatic stress. The recent advances proposed by local approaches may now overcome these shortcomings and provide useful tools. However, there is still a strong need for validations. This paper presents experimental and three-dimensional numerical studies conducted with the Rousselier model [2]. The objective is to evaluate the ability of such a model to describe crack initiation and growth. The results are interpreted in terms of stress triaxiality and global quantities issued from global approaches.

2 MODIFIED ROUSSELIER MODEL

In the following paper, a damage model describing the micro-mechanical process of ductile fracture is used to simulate crack initiation and growth in both tensile and compact tension specimens. Ductile fracture occurs as a result of nucleation, growth and coalescence of voids present in the metal matrix [3], as shown in Figure 1. Void nucleation occurs essentially at second phase particles and can be described by the Beremin model [4], assuming that an equivalent stress reaches a critical value.

If the load continues to increase, void growth will directly follow from cavity formation. The Von Mises yield function is usually assumed to describe the elastoplastic behaviour of metals. However, as voids develop, the volume constancy no longer prevail. Furthermore, yielding can occur even in a pure macroscopic hydrostatic stress state since only a bi-axial stress state is possible on the surfaces of the voids. In contrast to the Von Mises yield function, these phenomenon are accounted for in the formulation of Rousselier [2] used in these investigations. The yield function is expressed by :

$$F = \frac{\sigma_{eq}}{1-f} + D\sigma_1 f \exp\left(\frac{\sigma_m}{(1-f)\sigma_1}\right) - R(p) \tag{1}$$

where σ_{eq} is the Von Mises stress, σ_m is the hydrostatic stress, f is the void volume fraction, $R(p)$ is the true stress-strain curve and D and σ_1 are constants resulting from the derivation of the model. From Equation 1, it appears that if f is set to zero, the plastic potential retrieves it's usual form confirming that the Rousselier model is an extension of the Von Mises yield criterion [5], as shown in Figure 2. Void coalescence is also implicitly included in the formulation of the Rousselier model : as damage increases for increasing values of load, the stresses drop with increasing strains, simulating void coalescence. Based on the observation that the stress drop is not steep enough and could be responsible for numerical errors when modelling large amounts of ductile crack growth [6], the model was modified by introducing a critical void volume fraction f_c. As the Gauss point void volume fraction reaches f_c, the material stiffness is set to zero resulting in a steep drop of stress to zero, as illustrated in Figure 3 for a smooth notched tension specimen. Similar techniques have used with other models [7].

3 DAMAGE MODEL PARAMETER IDENTIFICATION

3.1 Material

The material investigated in this study is a fine grained optimised highly ductile 20 MnMoNi 5 5 steel. All tests were performed at 80°C. At this temperature, the material is at the beginning of the upper shelf on the notch impact energy temperature curve ($A_v \approx 200$J). The chemical composition of the material is given in Table 1 and the characteristic material parameters at the temperature under consideration are given in Table 2. The material stress-strain curve determined from tensile tests and used in the calculation is shown in Figure 4.

3.2 Model parameters

The damage model parameters were identified from both metallographical analysis of the material and experimental results obtained with round notched tensile and fracture mechanics specimens. Rather than using Franklin formulae [8] (only applicable to pure manganese sulphides inclusions) for determining the initial void volume fraction f_o, image processing of metallographic analyses of the material matrix was used to determine the volume fraction of inclusion f_v. Since the observations revealed spherical inclusions, the value of f_o was taken equal to f_v and then adjusted by comparing the results of FE calculations with the load versus diametral contraction measured on round notched tensile specimen, as recommended in [9]. The best agreement was obtained for $f_o = 1.8\ 10^{-4}$. As acknowledged in the literature [6], the integration constant D was set to 2. The σ_1 value was set to a value equal to 2/3 the flow stress, corresponding to σ_1 = 445 MPa and a value f_c of 0.05, widely used at MPA Stuttgart, was assumed.

For fracture mechanics calculation, l_c (corresponding one half of the length of the square elements used to model the region of crack growth) is a material constant. It was determined both from metallographic observations (image processing of the material matrix to determine the averaged distance between inclusions) and from comparison between calculated and experimental crack growth data from fracture mechanics specimens (CT25 and TPB25 specimens). The best results were obtained for l_c = 0.21 mm.

4 NUMERICAL STUDIES

The finite element code CASTEM 2000 [10] developed by CEA in France was used throughout the study. Both a non side-grooved and a 20% side-grooved CT25 specimens were simulated in the study. For the side-grooved specimen, a 2D simulation (plane strain conditions) and a 3D simulation modelling in detail the side-grooves were conducted. The modelled CT specimen has a a_0/W ratio of 0.586 and the results of 2 experiments are available for comparison. A radius of 0.1mm was assumed at the side-groove in the model. For the non side-grooved specimen, only a 3D analysis can be carried out due to the changing stress state over the specimen thickness. The curved cracked front, resulting from fatigue pre-cracking was measured and accounted for in the model. Four specimens were available for comparison with a a_0/W ratio ranging from 0.544 to 0.574. In all simulations, large displacements and large strain theory were assumed.

The calculated and experimental load versus CMOD curves for the 20% side-grooved specimens are shown in Figure 5. It is clear that the elastoplastic simulation (2D simulation assuming plane strain conditions shown in white squares) can only predict the linear and the beginning of the non-linear macroscopic behaviour since crack growth is not accounted for. With the Rousselier model, accounting for crack growth, the numerical results are found to be in agreement within less than 5% with the experimental data. The maximum load is predicted with a maximum relative error of 0.5% in comparison with the experimental data. Similar results were obtained for the non side-grooved specimen.

The simulated CMOD versus Δa curves are compared with the experimental data in Figure 6 for both the 20% and the non side-grooved specimens. In the experiments, the Δa values were determined using 20% unloading and measurement of the compliance, as it can be observed in Figure 5. There is a good agreement between the simulated results and the experimental data. The model is not only able to provide a good description of the macroscopic behaviour of the specimens but also to produce a good description of crack growth. Distinctive results are obtained for the two specimens. The calculated crack shapes are compared with the experimental one in Figure 7. For the side-grooved specimen, the crack grows uniformly through the specimen thickness. At the side-groove, slightly more crack growth is obtained than at the mid-thickness of the specimen. This correlates very well with the experimental observations. For the non side-grooved specimen, a pronounced tunnelling effect is predicted, in excellent agreement with the experiment. Striction at the free face is also well predicted with this model.

5 DISCUSSION

The differences that can be observed on the J-Δa curves obtained experimentally for different specimens and components can be interpreted in terms of stress triaxiality through a multiaxiality factor q defined as [1] :

$$q = \frac{\sigma_v}{\sqrt{3}\sigma_m} \tag{2}$$

where σ_v is the Von Mises stress and σ_m is the hydrostatic stress. A high degree of stress mutiaxiality implies a low value of q whilst a low degree of stress triaxiality implies a high value of q. Side-grooved CT specimens are known to exhibit high stress triaxiality since this geometry does not favours much plasticity. It therefore accelerates crack growth and relatively flat J-Δa curves are to be expected. For TPB specimens (three point bend specimens), low stress triaxiality prevails allowing more plasticity resulting in slower crack growth and higher J-Δa curves than for CT specimens. For a non side-grooved CT specimen, stress triaxiality vary significantly through the thickness. This is illustrated in Figure 8 where the q factor for a CMOD = 1mm is plotted as a function of initial crack front distance at different thickness positions. For the 20% side-grooved specimen, approximately constant stress triaxiality is obtained whereas it is shown that it varies significantly for the non side-grooved specimen.

The influence of multiaxiality on the J-Δa curves was examined for the non side-grooved specimen. The J-integral distributions through the specimen thickness as a function of applied displacement are shown in Figure 9. It shows that higher values of J prevail at the specimen mid-thickness, corresponding to the location where higher degree of multiaxiality is observed. Closer to the free-face of the specimen, lower values of J are predicted corresponding to lower degree of multiaxiality. Just on the free face, unexpectedly higher J values were obtained which may result from large amounts of striction leading to crack branching at 45°, as observed in the experiments.

The experimentally determined J-Δa curves (ASTM E813-89 standard [11]) are compared to the predicted ones in Figures 10 and 11 for the 20% and non side-grooved specimens, respectively. A good agreement is obtained between the experimental results and the numerical data. The results confirm that with lower stress multiaxiality as obtained for the non side-grooved specimen, higher J-Δa curves are to be expected than for the side-grooved specimen that exhibits high stress mutliaxiality over the all thickness. The Rousselier model accounts for such effects.

The model can also predict crack initiation assuming that crack initiation occurs as the first gauss point in the model becomes fully damaged, i.e. the void volume fraction f reaches the critical void volume fraction f_c. Based on that definition, the numerical results shown in Figures 10 and 11 are in good agreement with the experimental J_i value determined in the experiment from an analysis of the stretched zone Δ_{ai} [12]. This J_i value appears to be independent of the geometry and confirms results obtained for other materials and geometries reported in [13].

6 CONCLUSIONS

Three dimensional analyses of ductile crack growth in CT specimens were carried out using the Rousselier model. It is shown that the model can account for varying stress triaxiality conditions and successfully describe complex crack growth situations. With such a model, it is possible to predict J-Δa curves in good agreement with experimental data. It confirms that crack initiation is independent of geometry. There is still however a strong need to evaluate the ability of such a model to describe the failure behaviour of industrial components.

REFERENCES

[1] **Clausmeyer, H., Kussmaul, K. and Roos, E.,** 1991, *Influence of the Stress State on the Failure Behaviour of Cracked Components Made of Steel*, Applied Mechanics Review, 44, 77-92.

[2] **Rousselier, G.,** 1986, *Les Modèles de Rupture Ductile et leurs Possibilités Actuelles dans le Cadre de l'Approche Locale*, EDF, Service Réacteurs Nucléaires et Echangeurs, Les Renardières, BP 1, F-77250, MORET-SUR-LOING, FRANCE.

[3] **Kussmaul, K., Eisele, S. and Seidenfuss, S.,** 1993, *On the Applicability of Local Approaches for the Determination of the Failure behaviour of Ductile Steels*, Journal of Pressure vessels and technology, Transaction of the ASME, 115, 214-220.

[4] **Beremin, F.M.,** 1981, *Study of Fracture Criteria for Ductile Rupture of A508 Steel*, 5th International Conference on Fracture, 29/03-3/04, Cannes, FRANCE.

[5] **Roos, E., Seidenfuss, M., Kramer, D., Krolop, S., Eisele, U. and Hindenlang, U.,** 1991, *Application and Evaluation of Different Methods for Determining Crack Resistance Curves*, Nuclear Engineering and Design, 130, 297-308.

[6] **Seidenfuss, M.,** 1992, *Untersuchungen zur Beschreibung des Versagensverhaltens mit Hilfe von Schadigungsmodellen am Beispiel des Werkstoffes 20 MnMoNi 5 5*, PhD Thesis, MPA Stuttgart, GERMANY.

[7] **Devaux, J., Joly, P. and Leblond, J.B.,** 1995, *Simulation by the Local Approach of the Ductile Crack Growth in a Pressure Vessel Steel using an Improved Gurson Tvergaard Model*, 21st MPA Seminar, 5-6/10, Stuttgart, GERMANY.

[8] **Franklin, A.G.,** 1969, *Comparison Between a Quantitative Microscope and Chemical Methods for Assessment of Non-Metallic Inclusions*, Journal of the iron and Steel Institute.

[9] **Bethmont, M., Rousselier, G., Kussmaul, K., Sauter, A. and Jovanovic, A.,** 1988, *The Method of Local Approach of Fracture and its Application to a Thermal Shock Experiment*, 14th MPA Stuttgart Seminar, 6-7/10, GERMANY.

[10] **CASTEM 2000,** 1996, Commissariat à l'Energie Atomique, DRN/DMT/SEMT/LAMS, F-91191, GIF-SUR-YVETTE, FRANCE.

[11] **ASTM E813-89,** 1988, *Standard Test method for J_{IC}, a Measure of Fracture Toughness*, Annual Book of ASTM Standards, 3.1.

[12] **Roos, E. and Eisele, U.,** 1988, *Determination of Material Characteristics Values in Elastic-Plastic fracture mechanics by Means of J-integral crack resistance Curve*, Journal of Testing and Evaluation, 16, 1-11.

[13] **Pitard-Bouet, J.M., Seidenfuss, M., Bethmont, M. and Kussmaul, K.,** 1996, *Experimental Investigations on the Shallow Crack Effect, on the 10 MnMoNi 5 5 Steel, and Computational Analysis in the Upper Shelf by Means of the Global and Local Approaches*, 22nd MPA Stuttgart Seminar, 10-11/10, GERMANY.

TABLES

C	Si	Mn	P	S	Cr	Mo	Ni	Al	Cu	V	Sn	Co	As	Ta
0.19	0.25	1.38	0.008	0.006	0.09	0.5	0.76	0.026	0.05	<0.01	-	0.011	-	<0.005

Table 1 : 20 MnMoNi 5 5 material chemical composition.

T_{NDT}	A_v	R_e	R_m	E	J_i	Δ_{ai}	$CTOD_i$	J_{IC}
-20 °C	200 J	395 N/mm^2	519 N/mm^2	207 000 N/mm^2	271.4 N/mm	0.163 mm	0.32 mm	628 N/mm

Table 2 : 20 MnMoNi 5 5 material characteristics at 80°C in the *T-S* orientation.

FIGURES

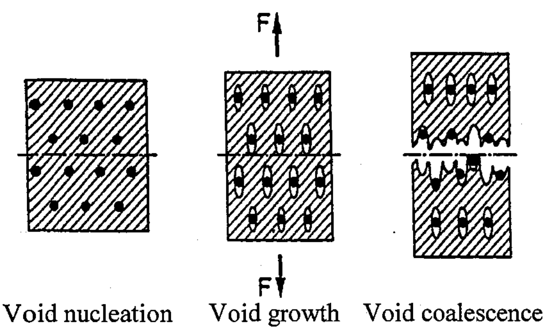

Figure 1 : The three elementary stages of ductile fracture.

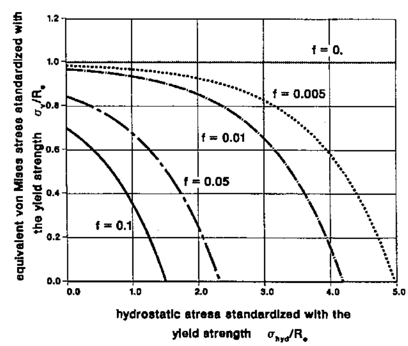

Figure 2 : Dependence of the Rousselier yield function on the hydrostatic stress for different void volumes (from [5]).

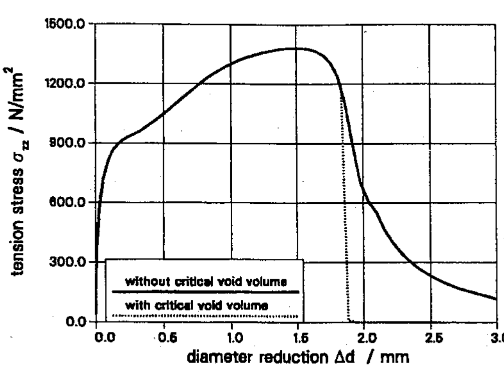

Figure 3 : Calculated axial stress in the centre of a round notched tensile specimen (from [6]).

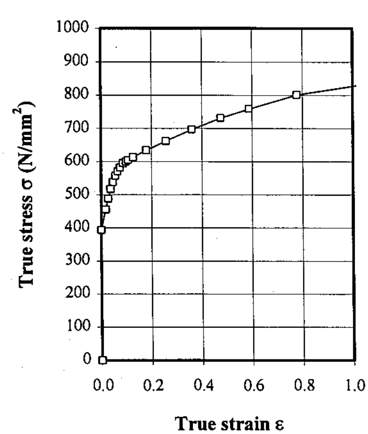

Figure 4 : 20 MnMoNi 5 5 true stress-strain curve at 80°C.

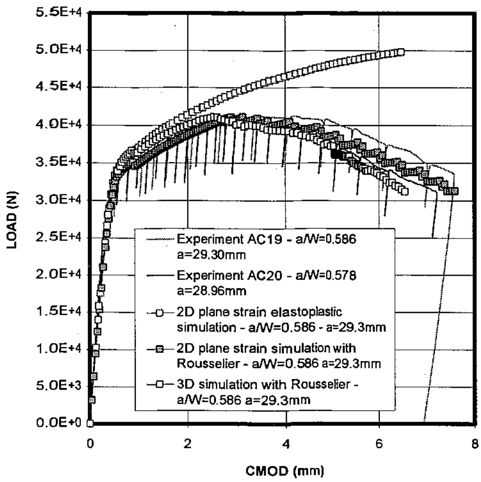

Figure 5 : Comparison between the calculated and the experimental load versus CMOD curve for the 20% side-grooved CT25 specimens.

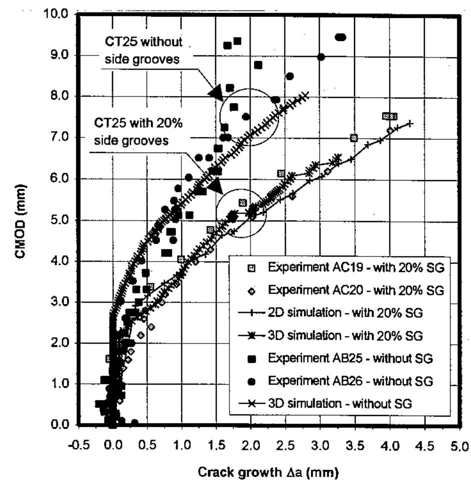

Figure 6 : Comparison between the calculated and the experimental CMOD versus Δa curve for the 20% and a non side-grooved CT25 specimens.

(a) Without side grooves

(b) with 20% side grooves

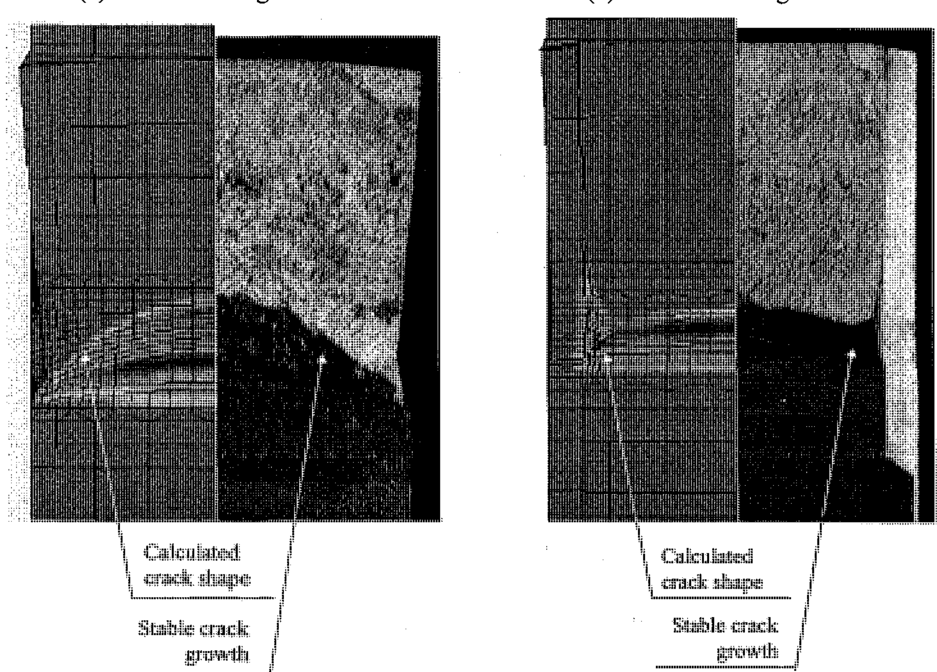

Figure 7 : Comparison between calculated and experimental crack shapes for 2 CT25 specimens (a) without side grooves and (b) with 20% side grooves.

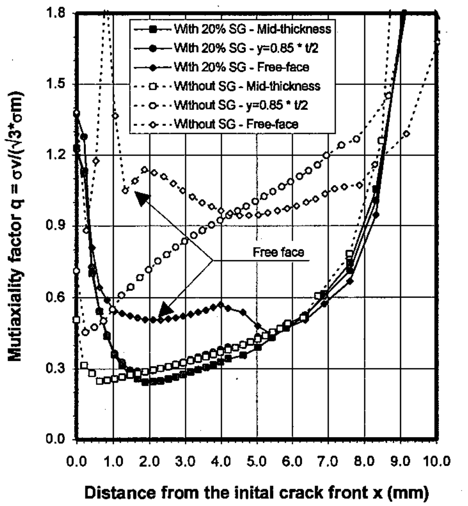

Figure 8 : Comparison between the multiaxiality factor q distribution through the specimen thickness for 20% and non side-grooved CT25 specimens (CMOD=1.0mm).

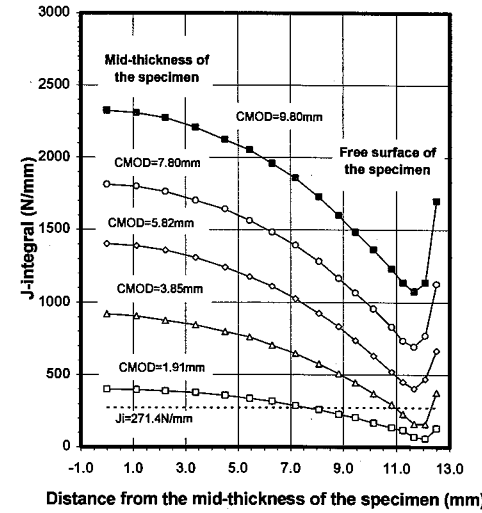

Figure 9 : J-integral distribution through the thickness as a function of applied displacement for a non side-grooved CT25 specimen.

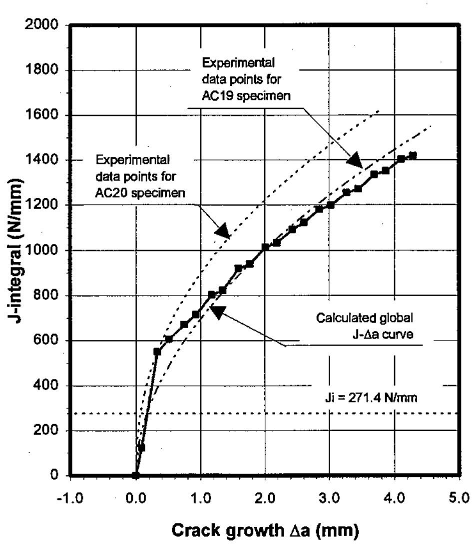

Figure 10 : Comparison between calculated and experimentally determined J-Δa curves for a 20% side-grooved CT25 specimen.

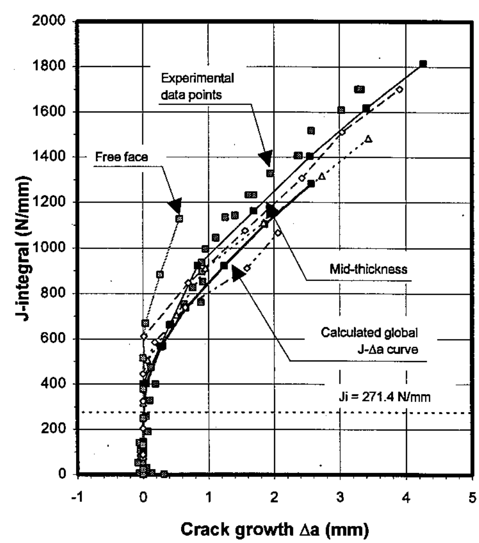

Figure 11 : Comparison between calculated and experimentally determined J-Δa curves for a non side-grooved CT25 specimen.